ELSEVIER

Advances in Colloid and Interface Science 132 (2007) 51 – 68

ADVANCES IN COLLOID AND INTERFACE SCIENCE

www.elsevier.com/locate/cis

Microtextured superhydrophobic surfaces: A thermodynamic analysis

W. Li, A. Amirfazli *

Department of Mechanical Engineering, University of Alberta, Edmonton, AB, Canada T6G 2G8

Available online 24 January 2007

Abstract

Superhydrophobic surfaces with a contact angle (CA) larger than 150° have recently attracted great interest in both academic research and practical applications due to their water-repellent or self-cleaning properties. However, thermodynamic mechanisms responsible for the effects of various factors such as surface geometry and chemistry, liquids, and environmental sources have not been well understood. In this study, a pillar microtexture, which has been intensively investigated in experiments, is chosen as a typical example and thermodynamically analyzed in detail. To gain a comprehensive insight into superhydrophobic behavior, the roles of pillar height, width and spacing (or roughness and solid fraction), intrinsic CA, drop size, and vibrational energy are systematically investigated. Free energy (FE) and free energy barrier (FEB) are calculated using a simple and robust model. Based on the calculations of FE and FEB, various CAs, including apparent, equilibrium (stable), advancing and receding CAs, and contact angle hysteresis (CAH) can be determined. Especially, the design of practical superhydrophobic surfaces is emphasized in connection with the transition between noncomposite and composite states; a criterion for judging such transition is proposed. The theoretical results are consistent with the Wenzel's and the Cassie's equations for equilibrium CA values and experimental observations. Furthermore, based on these results and the proposed criterion, some general principles to achieve superhydrophobic performance are suggested.

Keywords: Superhydrophobic; Wetting; Contact angle; Contact angle hysteresis; Free energy; Energy barrier; Vibrational energy

Contents

* Corresponding author. Tel.: +1 780 492 6711; fax: +1 780 492 2200.
E-mail address: a.amirfazli@ualberta.ca (A. Amirfazli).

0001-8686/$ - see front matter © 2007 Elsevier B.V. All rights reserved.
doi:10.1016/j.cis.2007.01.001

1. Introduction

Inspired by the so-called lotus effect [1,2], superhydrophobic surfaces with water contact angles (CA) larger than 150° have attracted great interest over the last few years from both fundamental research and practical applications [3–9]. Such surfaces require both appropriate surface roughness and generally low surface energy. With rapid improvements of micro/nanofabrication techniques, it is now becoming possible to control and tailor micro/nano-scale chemical structures on solid surfaces. Numerous methods to prepare superhydrophobic surfaces have been reported. Some of the recent examples include using surface roughness as a means to switch wettability of membranes [10] and fabrication of stable ZnO-based superhydrophobic surfaces using a wet-chemical route [11]. However, in spite of significant advances in fabrication techniques for micro/nanostructures and development of novel materials for superhydrophobic surfaces, the thermodynamic mechanism responsible for superhydrophobic behavior has not been completely understood. It is generally accepted that superhydrophobicity can be described using a maximum CA; however, it should be recognized that only CA is not sufficient to define superhydrophobicity if drop mobility is to be considered; additionally, contact angle hysteresis values or the work of adhesion is required [12,13]. To design and fabricate superhydrophobic surfaces, the following are some of the most important issues that should be addressed and clarified theoretically.

1.1. Surface geometry

It is well known that generally low surface energy and suitable surface roughness can enhance contact angle (CA) of a solid surface. Lowering of surface energy is limited to well packed CF_3 groups at the surface, corresponding to a maximum intrinsic CA of about 120° with water [14]. Recent studies have focused on manipulating roughness to achieve superhydrophobic surfaces. However, for the same roughness value, different surface geometries (textures) can exhibit completely different wetting behavior. A typical surface with pillar (post or spike) microtextures, as illustrated in Fig. 1, has been extensively investigated experimentally [4–8,15]. It has been argued that all the geometrical parameters of pillars, such as height, cross section, and arrangement, individually play a role in determining superhydrophobic behavior. This indicates that the consideration of only roughness value (a composite measure of all surface texture parameters) is not adequate. For example, it is suggested [12,14] that thin and tall pillars are necessary for superhydrophobicity; however, in term of roughness, this is contradictory because thin pillars mean small roughness if pillar spacing is kept constant (based on general roughness parameters, e.g., Wenzel roughness ratio (see Eq. (17) below)), whereas tall pillars mean large roughness (see roughness expression below). Therefore, investigations of the effect of all surface geometrical parameters (height, cross section, and arrangement) are necessary. It is worth noting that the pillar texture is used in many recent experimental investigations of superhydrophobic behavior [17,18]. However, systematic and complete studies on the effects of all the geometrical parameters have not been conducted. For example, among the latest studies, Nakae et al. [16] investigated the effect of roughness pitch (i.e., pillar spacing); Callies et al. [17] investigated the effect of microstructure density in natural surfaces (also pillar spacing). However, such studies hardly consider theoretically why and how surface geometry impacts apparent, equilibrium (stable), advancing and receding CAs. It is therefore necessary to understand the fundamental mechanism responsible for the effects of surface geometry (rather than only the roughness value) and

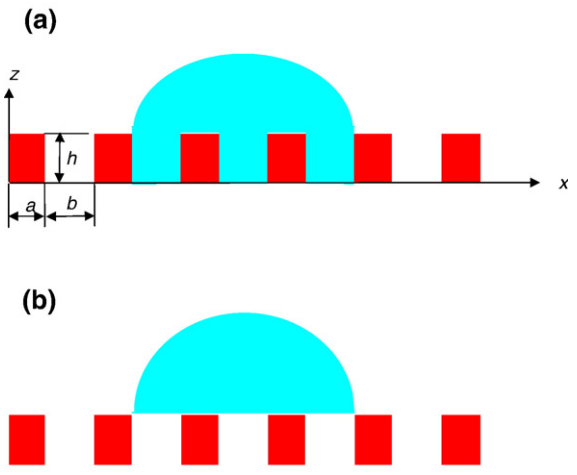

Fig. 1. A typical 2-D pillar surface microtexture. (a) noncomposite; (b) composite wetting states.

material chemistry, and their interrelation on superhydrophobicity. This issue is important for the geometrical design of superhydrophobic surfaces. At present, however, theoretical explorations of such effects are still rare (the notable examples are the latest study on the microscopic mechanism of the dependence of CA on roughness using a variational minimization of total potential energy [19], and the analysis of anisotropy in the wetting of rough surface using Surface Evolver [20]). Accordingly, up to now the guidelines for the fabrication of superhydrophobic surfaces have considered a general notion of roughness (not exact surface geometry), and are mainly based on experimental observations or phenomenological methodologies; rigorous and systematic theoretical consideration, in particular, thermodynamic analysis is rare.

1.2. Criterion for the transition from noncomposite to composite wetting states

A change in roughness or surface geometry (texture) may lead to a transition between thermodynamic states from noncomposite, i.e., complete liquid penetration into the troughs of a rough surface, to composite, i.e., entrapment of air in the troughs of a rough surface, as illustrated in Fig. 1. Such a transition may increase maximum CA and/or further enhance the superhydrophobicity. The equilibrium CAs for these two states can be evaluated by classical Wenzel's and Cassie's equations [21,22], but *a priori* it is difficult to predict which equation would apply to a particular system [5,6,23]. A wetting system may exhibit both states for a given situation; a transition between noncomposite and composite states can also occur with variations of surface conditions (e.g., composition and geometry). In general, this transition is the result of competition between noncomposite and composite thermodynamic states. The result of this competition is determined by the two factors of free energy (FE) and free energy barrier (FEB). A system always transfers to a thermodynamic state with a low FE with small transitional FEB. Depending on surface geometry and chemistry of a microtextured solid, one of the noncomposite or composite states has the lowest FE. A complete understanding on why and how surface geometry and chemistry affect the transition is essential for the design and prediction of superhydrophobic behavior. There have been considerable studies on determining this transition in the recent years. For example, Extrand [24] proposed a contact line density criterion to predict suspension of water drop on top of surface asperities; more recently, because of the inadequate validity for some experimental observations, he added an additional asperity height criterion for such transition [25]. However, models allowing for calculating/predicting such a transition, in particular, simple and reliable thermodynamic treatments are scarce.

1.3. Contact angle hysteresis (CAH)

In general, wetting behavior can be characterized commonly by a CA. However, maximum CA is insufficient to assess superhydrophobicity when drop mobility is desired [4,12]. A superhydrophobic surface suitable for liquid shedding should exhibit both high CA and low contact angle hysteresis (CAH), i.e., the difference between advancing or maximum (θ_a) and receding or minimum (θ_r) CAs. Recently, maximum CA of various materials and associated superhydrophobic behavior has been widely investigated, but the CAH is studied so far only to a very limited extent, in particular, from theoretical aspects [15,26,27]. In spite of its important role in determining superhydrophobic behavior, theoretically there is not a general or simple approach to predict CAH due to its complexity (Wenzel's and Cassie's models can predict equilibrium CA of noncomposite and composite states, respectively, but neither equation can predict CAH). This happens partly because the CAH is non-intrinsic property of a solid surface, which is, in some sense, dependent on the concerned system or environment (see below). In principle, CAH can be calculated by analyzing the thermodynamic status of a system consisting of a solid surface and a liquid drop. This was well demonstrated by Johnson and Dettre (J–D) in their classical work [28]. Unfortunately, their numerical calculations were cumbersome and complicated; also, their model used a sinusoidal roughness pattern for the surface, which is not very realistic or achievable by current microfabrication techniques. Recently, some researchers have used empirical or phenomenological models [5–7,24] to approach CAH. Although the above studies were in agreement with specific experimental observations, and advanced our understanding of the CAH for superhydrophobic surfaces, generally, they could not be considered as being rigorously derived from first principles of thermodynamics (e.g., FE analysis for metastable states). To better understand and evaluate the superhydrophobicity, it is necessary to develop a simple and general thermodynamic approach to calculate CAH.

1.4. The effect of drop size

The factors such as the formation and the size of a drop can play a significant role in the observed CA. For example, different wetting behavior is observed by depositing a drop gently, from some height or pushing it by applying pressure on a solid surface [29]. Especially, experimental evidence regarding the effect of drop size on CAs has been well documented [30–32]. However, the only theoretical consideration was conducted by Marmur [33] who proposed a simple model of heterogeneous smooth surfaces to demonstrate the possible effects of drop volume on the metastable states of a thermodynamic system. Thus, to systematically investigate superhydrophobic behavior the issue of drop size should be addressed.

1.5. The effect of external environment

Environmental or external sources such as temperature, mechanical vibrations, light and acoustical energy may play a role in determining superhydrophobic behavior. In this aspect, Johnson and Dettre [28] made an important contribution by revealing the significance of the so-called "vibrational energy". Vibrational energy is defined as the energy to overcome FEB. Here it should be pointed out that in general sense, the vibrational energy means the energy that a wetting system receives from its environment or external sources, e.g., mechanical

vibrations of the building in which the experiments are done, acoustical or light; the "vibrational energy" in our case does not refer to the vibration at a molecular level for the system (the examples of vibrational energy concerned here can be found in [34,36]). It is experimentally found that the vibrational energy can impose practical bounds on measurements of CA [34]. In general, the higher the vibrational energy, the smaller the practical range of the observed CAs or CAH. If the vibrational energy is large enough, only a stable or equilibrium CA rather than a range of CAs (i.e., CAH) can be experimentally observed. There have been experimental studies to demonstrate this point; mechanical or acoustical means such as direct vibration of a solid surface or application of a loudspeaker in order to create large vibrational energy was used [34–36]. Noblin et al. [37] showed that the contact line can either remain pinned or oscillate, depending on the frequency and the amplitude of the vibration; the hysteresis acts as a frictional force, leading to a stick slip motion of the triple line. Such studies support the basic assumption that CAH depends on the vibrational energy from external sources. At present, in the study of superhydrophobic phenomenon, it is urgent to establish the relationship between vibrational energy and CAs, as well as CAH.

It should be pointed out that external sources may also lead to the change in surface conditions such as composition (chemistry) and structure (roughness), causing changes in wetting properties (e.g., variation in CA) [38,39]. For instance, an extremely large change in CA or CAH of aligned ZnO nanorod films can be realized using ultraviolet irradiation [39]. Such a change in CA can be generally understood by the interplay of surface chemistry and roughness with external stimulus, and not the manifestation of "vibrational energy" from external sources such as building vibrations discussed here.

1.6. Thermodynamic analysis of superhydrophobic surfaces

In view of the above considerations, superhydrophobic behavior can be affected by multiple factors. Although superhydrophobicity is necessarily characterized using CA, it is difficult and complex to make meaningful CA measurements and to reveal the physical nature of the measurements for superhydrophobic behavior. It is therefore, understandable why a wide range of CA values are presented in literature by different researchers even on the same solid surface [40]. Accordingly, there are considerable controversial assertions on the fundamental aspects of superhydrophobic phenomena. Some of the controversy is due to the lack of a theory/model that can quantitatively interpret experimental measurements of CA and CAH in terms of the contributions of surface chemistry and geometry, drop size, and external sources.

In our previous study [41], we proposed a thermodynamic approach to analyze FE and FEB of a metastable wetting state. In

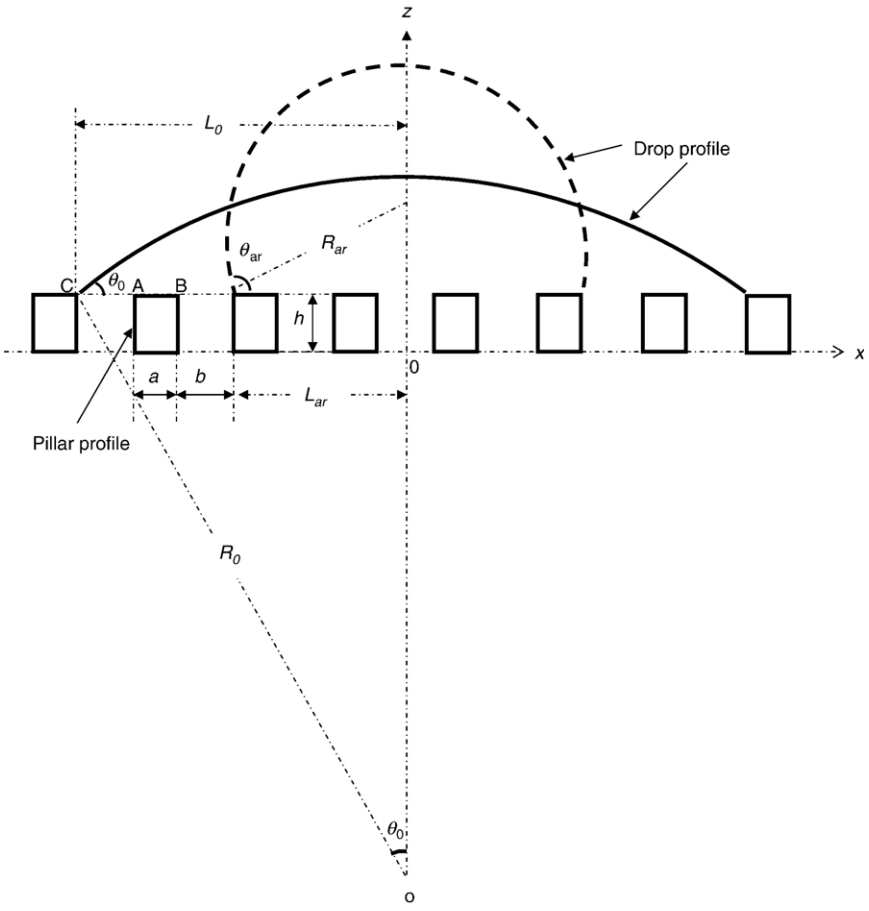

Fig. 2. Illustration of FE analysis for a drop on a surface with a pillar texture. Solid line represents the initial state of the drop whereas dashed line is to signify an arbitrary state of the drop.

this approach, we proposed a two-dimensional model assuming cylindrical drops and neglecting the gravity effect to simplify the calculations of CA and CAH associated with FE and FEB without much loss of generality as the results can describe experimental observations clearly. In the present study, using this approach we conduct a detailed analysis of a typical surface with a pillar microstructure. The aim is to provide a comprehensive understanding of the roles of various factors, including chemistry (intrinsic CA), surface geometry (solid fraction and roughness), liquid (drop size or volume), and external means (vibrational energy) in determining superhydrophobic behavior, i.e., CA and CAH as well as the transition from noncomposite to composite states. The final aim is to provide some guidelines for the design of superhydrophobic surfaces.

2. Thermodynamic analysis

In our previous study [41], a FE analysis and formulation was presented for wetting of a surface with the texture shown in Fig. 1. The texture design in Fig. 1 is regularly used by experimentalists to study superhydrophobic phenomenon. The formulation provided allowed study of both noncomposite and composite wetting states. Based on the developed model, the thermodynamic analysis of the wetting states related to the surface texture geometry and numerical calculations of FE and FEB can be conducted. For a wetting noncomposite state, the change in FE per unit length of contact line (ΔF) for a drop receding from a reference position (with drop size and CA of L_0 and θ_0, respectively), to an arbitrary position with L_{ar} and θ_{ar}, can be written as (see Fig. 2):

$$\Delta F^{re}_{0\to ar}/\gamma^{la} = \left(\theta_{ar}\frac{L_{ar}}{\sin\theta_{ar}} - \theta_0\frac{L_0}{\sin\theta_0}\right) + \left(\frac{L_0 - L_{ar}}{a+b}\right)(a+b+2h)\cos\theta_Y \quad (1)$$

The equivalent change in FE per unit length of contact line (ΔF) for the advancing case will be:

$$\Delta F^{ad}_{0\to ar}/\gamma^{la} = \left(\theta_{ar}\frac{L_{ar}}{\sin\theta_{ar}} - \theta_0\frac{L_0}{\sin\theta_0}\right) - \left(\frac{L_0 - L_{ar}}{a+b}\right)(a+b+2h)\cos\theta_Y \quad (2)$$

where γ^{la} is liquid surface tension; a and b are defined in Fig. 2; $\Delta F/\gamma^{la}$ is the normalized change in FE per unit length of contact line or the so-called FEB; θ_Y is the intrinsic CA.

The variation of FE as a result of an infinite small change in drop position receding from point A (with drop size L_A and CA of θ_A) to the neighboring point B (with drop size L_B and CA of θ_B, where $L_A \approx L_B$ and $\theta_A \approx \theta_B$) can be expressed as follows for a noncomposite state:

$$\theta_A\frac{L_A^2}{\sin^2\vartheta_A} - L_A^2 ctg\theta_A = \theta_B\frac{L_B^2}{\sin^2\theta_B} - L_B^2 ctg\theta_B \quad (3)$$

$$\Delta F_{A\to B}/\gamma^{la} = \left(\theta_B\frac{L_B}{\sin\theta_B} - \theta_A\frac{L_A}{\sin\theta_A}\right) + a\cos\theta_Y \quad (4)$$

Eq. (3) is a geometrical constraint as a result of constant drop volume assumption between two neighboring states. The equivalent equations for the advancing case from A to the neighboring point C (with drop size L_C, and CA of θ_C) can be expressed as:

$$\theta_A\frac{L_A^2}{\sin^2\vartheta_A} - L_A^2 ctg\theta_A = \theta_C\frac{L_C^2}{\sin^2\theta_C} - L_C^2 ctg\theta_C + 2bh \quad (5)$$

$$\Delta F_{A\to C}/\gamma^{la} = \left(\theta_C\frac{L_C}{\sin\theta_C} - \theta_A\frac{L_A}{\sin\theta_A}\right) - (b+2h)\cos\theta_Y \quad (6)$$

where h is pillar height as shown in Fig. 2.

For the case of a composite system, liquid does not penetrate into the troughs. The change in FE can be easily derived using the same method. When the drop recedes or advances from the reference position to an arbitrary position, the geometrical constraint and energy equations associated with the changes in FE per unit length of contact line (ΔF), respectively, can be derived as Eqs. (7)–(9).

$$\theta_0\frac{L_0^2}{\sin^2\theta_0} - L_0^2 ctg\theta_0 = \theta_{ar}\frac{L_{ar}^2}{\sin^2\theta_{ar}} - L_{ar}^2 ctg\theta_{ar} \quad (7)$$

$$\Delta F^{re}_{0\to ar}/\gamma^{la} = \left(\theta_{ar}\frac{L_{ar}}{\sin\theta_{ar}} - \theta_0\frac{L_0}{\sin\theta_0}\right) - \left(\frac{L_0 - L_{ar}}{a+b}\right)(b - a\cos\theta_Y) \quad (8)$$

$$\Delta F^{ad}_{0\to ar}/\gamma^{la} = \left(\theta_{ar}\frac{L_{ar}}{\sin\vartheta_{ar}} - \theta_0\frac{L_0}{\sin\theta_0}\right) + \left(\frac{L_0 - L_{ar}}{a+b}\right)(b - a\cos\theta_Y) \quad (9)$$

Similarly, the geometrical constraint and energy equations associated with the two FEBs for the composite state can also be derived; note that for the receding case, the derived geometrical constraint and energy equations for the composite state are the same as those for the noncomposite state (i.e., Eqs. (3) and (4)), whereas for the advancing case, the derived geometrical constraint and energy equations for the composite state are as follows:

$$\theta_A\frac{L_A^2}{\sin^2\theta_A} - L_A^2 ctg\theta_A = \theta_C\frac{L_C^2}{\sin^2\theta_C} - L_C^2 ctg\theta_C \quad (10)$$

$$\Delta F_{A\to C}/\gamma^{la} = \left(\theta_C\frac{L_C}{\sin\theta_C} - \theta_A\frac{L_A}{\sin\theta_A}\right) + b \quad (11)$$

2.1. The FE analysis for the transition between noncomposite and composite wetting states

Superhydrophobic states are thermodynamic manifestation of FE. By comparing the FE of noncomposite and composite states, one can determine which state is energetically favorable. Here we derive the FE change for the transition from a noncomposite to a composite state. Consider a noncomposite state associated with a drop width (L_{nc}) and a CA (θ_{nc}), as illustrated in Fig. 3. When such system exhibits a composite state associated with an equivalent drop width ($L_{com}=L_{nc}$) and a

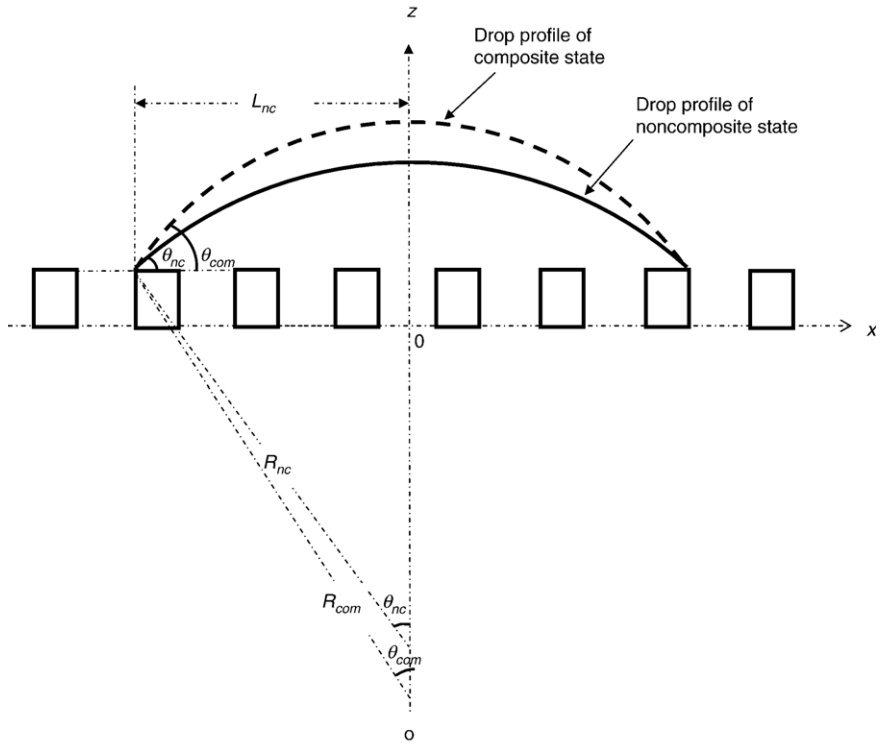

Fig. 3. Illustration of FE analysis for the transition between noncomposite and composite states (note drop volume is considered constant for both states).

CA (θ_{com}), the FE per unit length of contact line, F, for these two states can be expressed as:

$$F_{\mathrm{nc}} = \gamma^{\mathrm{la}} l_{\mathrm{nc}}^{\mathrm{la}} + \gamma^{\mathrm{ls}} l_{\mathrm{nc}}^{\mathrm{ls}} + C_2 \tag{12}$$

$$F_{\mathrm{com}} = \gamma^{\mathrm{la}} l_{\mathrm{com}}^{\mathrm{la}} + \gamma^{\mathrm{sa}} l_{\mathrm{com}}^{\mathrm{sa}} + C_2 \tag{13}$$

where C_2 is the FE of the portion of the system that remains unchanged as a result of the transition between noncomposite and composite states. Note that given the geometry of the system studied, the following relationships exist: $l_{\mathrm{nc}}^{\mathrm{la}} = \theta_{\mathrm{nc}} L_{\mathrm{nc}}/\sin\theta_{\mathrm{nc}}$, $l_{\mathrm{nc}}^{\mathrm{ls}} = \left(\frac{L_{\mathrm{nc}}}{a+b}\right)(b+2h)$, $l_{\mathrm{com}}^{\mathrm{la}} = \theta_{\mathrm{com}} L_{\mathrm{com}}/\sin\theta_{\mathrm{com}} + \left(\frac{L_{\mathrm{com}}}{a+b}\right)(b+2h)$, and $l_{\mathrm{com}}^{\mathrm{sa}} = \left(\frac{L_{\mathrm{com}}}{a+b}\right)(b+2h)$. Applying the constant drop volume constraint or its 2D equivalent, constant drop area in x-z plane allows derivation of Eq. (14) as:

$$\theta_{\mathrm{nc}} \frac{L_{\mathrm{non}}^2}{\sin^2\theta_{\mathrm{nc}}} - L_{\mathrm{nc}}^2 \mathrm{ctg}\theta_{\mathrm{nc}} + \frac{L_{\mathrm{nc}}}{(a+b)} bh = \theta_{\mathrm{com}} \frac{L_{\mathrm{com}}^2}{\sin^2\theta_{\mathrm{com}}} - L_{\mathrm{com}}^2 \mathrm{ctg}\theta_{\mathrm{com}} \tag{14}$$

Because Young's equation is locally valid, the FE change for the transition from a noncomposite state to a composite state can be expressed as Eq. (15).

$$\Delta F_{\mathrm{nc}\to\mathrm{com}}/\gamma^{\mathrm{la}} = \left(\theta_{\mathrm{com}} \frac{L_{\mathrm{com}}}{\sin\theta_{\mathrm{com}}} - \theta_{\mathrm{nc}} \frac{L_{\mathrm{nc}}}{\sin\theta_{\mathrm{nc}}}\right) + \frac{L_{\mathrm{nc}}}{a+b} b + \frac{L_{\mathrm{com}}}{a+b}(b+2h)\cos\theta_Y \tag{15}$$

2.2. Calculations of equilibrium CA, receding and advancing CAs, and CAH

From a thermodynamic point of view, a wetting system with an equilibrium CA should exhibit the lowest FE state. However, such a system can also exhibit multi-valued FE property, implying the existence of multiple metastable equilibrium states. This explains the thermodynamic conditions for existence of advancing and receding CAs and their manifestation CAH (each metastable state is associated with an apparent CA). Accordingly, a thermodynamic model should be capable of analyzing the metastable states and to calculate the related CAs and CAH. In principle, the present model may allow analytical determination of the multiple minima for FE. In the present study, there are two types of equations: energy and geometry related. Differentiation of an energy equation yields the FE minima whereas the geometrical variables in the energy equations are subjected to the constraint of the geometrical equations (e.g. constant liquid volume). Here we show a simple example. In case of the receding in a noncomposite state, based on Eq. (1), the differential of ΔF with respect to CA will be:

$$\frac{\mathrm{d}(\Delta F_{0\to\mathrm{ar}}^{\mathrm{re}}/\gamma^{\mathrm{la}})}{\mathrm{d}(\theta_{ar})} = \frac{L_{ar}}{\sin\theta_{ar}} + \frac{\theta_{ar}}{\sin\theta_{\mathrm{ar}}} \frac{\mathrm{d}(L_{\mathrm{ar}})}{\mathrm{d}(\theta_{\mathrm{ar}})} - \frac{\theta_{\mathrm{ar}} L_{\mathrm{ar}} \cos\theta_{\mathrm{ar}}}{\sin^2\theta_{\mathrm{ar}}} - \frac{\cos\theta_Y}{a+b} \frac{\mathrm{d}(L_{\mathrm{ar}})}{\mathrm{d}(\theta_{\mathrm{ar}})} \tag{16}$$

It is noted that because L_{ar} is also a function of θ_{ar}, it might be possible but difficult to obtain an analytical solution for Eq. (16). However, it is easier to conduct numerical calculations.

For various θ_{ar} values representing the range of possible CA between advancing and receding values, using FE or FEB equations, the change in FE or FEB can be calculated. Fig. 4 shows a typical bowl-shaped curve of FE as a function of apparent CA (θ_{ar}) for a noncomposite state ($a=b=2\times10^{-6}$, $h=0.75$ μm); note that FE as described above (i.e., F per unit length of contact line) is normalized with respect to γ (the FE unit will then be meter) [41]. As shown, the absolute or global minimum, i.e., the point of lowest FE associated with an equilibrium CA can be found.

Based on the geometrical dimension of the surface microstructure, Wenzel's roughness ratio (r) can be expressed as:

$$r = 1 + \frac{2h}{a+b} \tag{17}$$

Similarly, Cassie's solid fraction (f) can be expressed as:

$$f = \frac{a}{a+b} \tag{18}$$

Using Eqs. (17) and (18), in conjunction with the Wenzel and the Cassie equations (i.e. $\cos\theta_w = r\cos\theta_Y$ and $\cos\theta_c = f\cos\theta_Y + f - 1$, respectively), the CAs for the above geometrical system ($a=b=2\times10^{-6}$, $h=0.75$ μm) can be calculated as: $\theta_w=133.8°$; and $\theta_c=138.6°$. It is important to note that the equilibrium CA in Fig. 4 exactly corresponds to Wenzel's CA.

The curve shown in Fig. 4 is smooth with variations in CA and has only one minimum i.e., the global FE value. However, if θ_{ar} changes slightly on the order of 10^{-2} degree (e.g., drop moves from a pillar edge position to another neighboring position such as from A to B or C in Fig. 2), the local curve can show a fluctuation in FE, as illustrated in the inset of Fig. 4. These fluctuations demonstrate multiple local minima points in FE. As indicated before, each minimum represents a metastable state, associated with a corresponding apparent CA (θ_{ar}). On each side of a local minimum, there are always two FEBs, (one associated with retreating contact line, Δ_{AB} in Fig. 4 and another with a advancing contact line Δ_{AC}). Note that given the geometry in Fig. 2, a retreating contact line leads to an increase in CA since drop volume is constant. This should not be confused with what is done in experiments to measure advancing and receding CAs, i.e. changing the volume of a sessile drop. In case of this thermodynamic calculation, here we are simply comparing the energy levels of two states for a drop with constant volume. Inevitably, the existence of these multiple metastable states can thermodynamically lead to the existence of multiple CA values, i.e., CAH for a wetting system. To obtain CAH or to calculate maximum (advancing) and minimum (receding) CAs, it is necessary to analyze these local minima of FE. According to the J–D model [28], a drop can rest in a metastable state with a non-zero FEB. In cases where the concerned system receives energy, i.e., the vibrational energy, from external sources, the drop can overcome the local FEB and move to another metastable state; if the vibrational energy is larger than all FEB present in a system, the drop will assume the equilibrium state (minimum FE). Therefore, the theoretical (or maximum) CAH, strictly speaking, is the value that is only observed under ideal conditions i.e., without the effect of external sources (any vibrations, air currents, temperature fluctuations etc.). In this case, the extreme advancing and receding CAs can be calculated using the zero FEB equations, i.e.,

$$\Delta F_{barrier} = f(\theta_{ar}) = 0 \tag{19}$$

Here we present a simple example. For a 2-D drop forming a noncomposite system and having a constant cross sectional area (A_0), based on Eq. (3) the receding CA (θ_r) should obey:

$$\theta_r \frac{L_r^2}{\sin^2\theta_r} - L_r^2 \mathrm{ctg}\theta_r = \theta_{r'} \frac{L_{r'}^2}{\sin^2\theta_{r'}} - L_r^2 \mathrm{ctg}\theta_{r'} = A_0 \tag{20}$$

where $L_{r'}=L_r+a$. From Eq. (20), an equation containing two variables θ_r and $\theta_{r'}$ can be derived as :

$$\left(\frac{\theta_{r'}}{\sin^2\theta_{r'}} - \frac{\cos\theta_{r'}}{\sin\theta_{r'}}\right)\left\{\left(\frac{A_0\sin^2\theta_r}{\theta_r - \sin\theta_r\cos\theta_r}\right)^{\frac{1}{2}} - a\right\}^2 - A_0 = 0 \tag{21}$$

Based on receding FEB Eq. (5), another equation that also contains two variables θ_r and $\theta_{r'}$ can be derived as:

$$\frac{\theta_{r'}}{\sin\theta_{r'}}\left\{\left(\frac{A_0\sin^2\theta_r}{\theta_r - \sin\theta_r\cos\theta_r}\right)^{\frac{1}{2}} - a\right\} - \frac{\theta_r}{\sin\theta_r}\left(\frac{A_0\sin^2\theta_r}{\theta_r - \sin\theta_r\cos\theta_r}\right)^{\frac{1}{2}} + a\cos\theta_Y = 0 \tag{22}$$

Solving for θ_r and $\theta_{r'}$, using Eqs. (21) and (22), the receding CA can be analytically obtained (θ_r or $\theta_{r'}$, both are approximately equal). Similarly, advancing CA can be found based on the Eqs. (5) and (6).

Fig. 5 shows the two curves corresponding to the advancing and receding FEBs (for $a=b=2\times10^{-6}$, $h=0.75$ μm); Fig. 5 is calculated using the geometrical and energy Eqs. (3)–(6). If the vibrational energy is assumed to have a value of zero, indicating that there is no FEB to advance or recede, the advancing and receding CAs as well as CAH can be determined by the intersecting values of advancing and receding curves with x-axis,

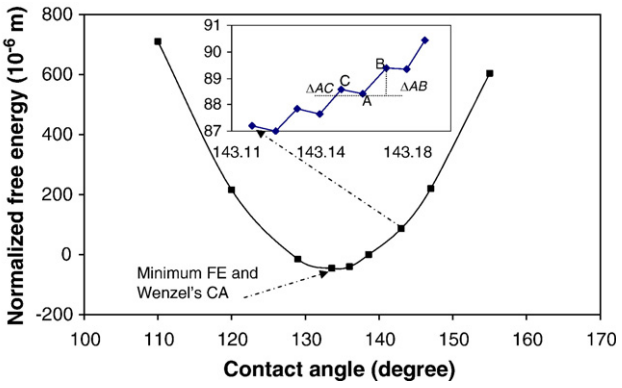

Fig. 4. Variation of normalized FE with CA for a noncomposite wetting state ($L=1\times10^{-2}$ m, $a=b=2$ μm, $h=0.75$ μm; intrinsic CA, i.e., $\theta_Y=120°$, $\theta_w=133.8°$). The inset shows an enlarge view of a segment of FE curve illustrating the FEB; positions A, B and C correspond to those in Fig. 2. Δ_{AB} and Δ_{AC} represent the FEB for retreating and advancing contact line, respectively; see Section 2.2. The lines are to guide the eyes.

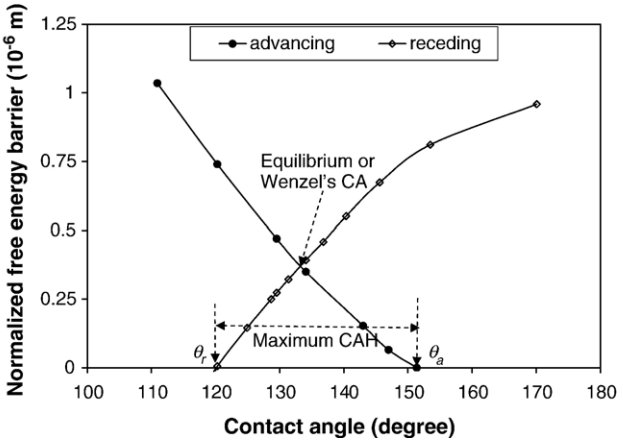

Fig. 5. Determining receding and advancing CAs as well as CAH from the typical curves of advancing and receding FEBs for a noncomposite wetting state ($L=1\times10^{-2}$ m, $a=b=2$ μm, $h=0.75$ μm; intrinsic CA, $\theta_Y=120°$). The CAH shown is the maximum value associated with zero FEB on the advancing and receding branches of the FE curve (see Fig. 4). The lines are to guide the eyes. FEB is per unit length of the contact line and it is normalized with respect to the surface tension of the liquid.

respectively (see Fig. 5). It is noted that the equilibrium CA can also be determined by FEB curves, i.e., the intersection point between advancing and receding curves in Fig. 5.

3. Results and discussion

The effect of surface texture geometry on superhydrophobic behavior is discussed first in terms of pillar height, spacing, and width (Fig. 1). The effect of chemical composition or its manifestation in terms of intrinsic CA is discussed next. The effect of drop size and vibrational energy is provided in Sections 3.4 and 3.5, respectively, followed by a discussion on concurrent effect of varying a number of parameters discussed in Section 3.6. In closing, basic guidelines for design of superhydrophobic surfaces are provided.

3.1. The effects of pillar height

The effect of pillar height is mainly discussed in our previous study [41], however, for completeness, it is briefly discussed here.

3.1.1. The effect of pillar height on FE

It is seen from Eq. (17) that for a given pillar width (a) and spacing (b), the role of Wenzel's roughness ratio in determining superhydrophobic behavior can be represented by that of pillar height (h). Fig. 6 illustrates comparison between FE variations for noncomposite and composite systems for various pillar heights. One can see that the composite state is more stable than noncomposite state as pillar height increases. For example, the FE of composite state is lower than that of noncomposite state when pillar height is above a critical pillar height, h_c (for condition given in Fig. 6, $h_c=1$ μm), whereas the opposite situations is true when pillar height is below h_c. It is important to note that the calculated equilibrium CA (with the lowest FE), θ_e, for noncomposite states depends strongly on pillar height and exactly corresponds to that predicted by Wenzel's equation (e.g., with $h=1.0$ μm: $\theta_e=\theta_w=138.6°$ or with $h=0.75$ μm: $\theta_e=\theta_w=133.8°$). The θ_e of composite state exactly corresponds to that predicted by Cassie's equation and does not depends on pillar height (e.g., $\theta_e=\theta_c=138.6°$ for both $h=1.0$ and $h=0.75$ μm). The necessity of a certain h value to allow transition from noncomposite to composite states and subsequent insensitivity to h value beyond h_c to maintain the composite state is also observed experimentally [15,18].

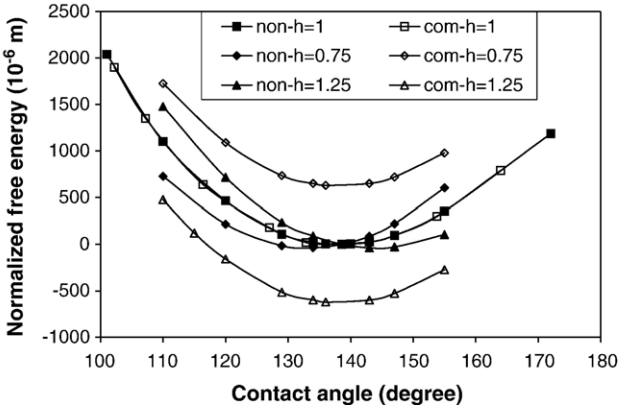

Fig. 6. Comparison of variations of normalized FE with apparent CA between noncomposite and composite wetting states with different pillar heights; the unit for h is micrometers; the other geometrical dimensions are: $L=1\times10^{-2}$ m, $a=b=2$ μm, intrinsic CA, $\theta_Y=120°$; *non* and *com* denote noncomposite and composite states, respectively. The lines are to guide the eyes [41].

3.1.2. The effect of pillar height on FEB and the transition between noncomposite and composite states

Fig. 7 shows the effect of pillar height on FEBs for noncomposite and composite wetting systems. One can see that FEB and the resultant CAH of composite system does not depend on pillar height. However, for noncomposite system, the FEB for an advancing case and the resultant CAH increases with pillar height,

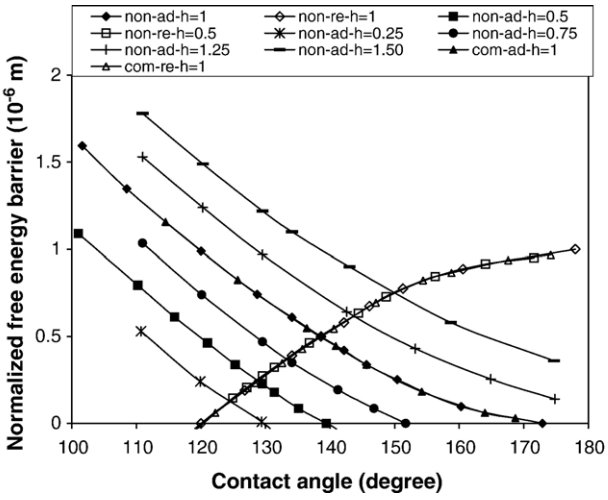

Fig. 7. Variations of normalized FEB with apparent CA for various pillar heights of the microstructure surfaces for noncomposite and composite wetting systems; $L=1\times10^{-2}$ m, $a=b=2$ μm, intrinsic CA, $\theta_Y=120°$; the unit for h is micrometers; *non* and *com* denote noncomposite and composite states; *re* and *ad* denote receding and advancing, respectively. The lines are to guide the eyes [41].

whereas the FEB for the receding case remains the same/constant. The present results reveal that the essential effect of pillar height is to promote the transition between noncomposite and composite states; pillar height does not affect CAH, as long as the composite state is maintained for a given pillar size and spacing; this is consistent with the experimental findings [43]. If pillar height is too small, the system will prefer noncomposite state, and its CAH strongly depends on pillar height (the limiting case of $h=0$ will result in zero CAH as expected for an ideally smooth surface). This is also supported by recent experimental observations. For instance, in [43], it was shown that CAH depended strongly on the height of surface texture (made of nanotubes) when noncomposite state was observed.

A critical height, therefore, can be found where both FE and FEB of noncomposite and composite states would be equal (e.g., for the system here, $h_c=1.0$ μm). As a result, a criterion for transition from noncomposite to composite can be found as:

$$h>h_c \tag{23}$$

Based on the above criterion, the variations of CAH with respect to pillar height for the studied geometrical microstructure ($a=b=2$ μm) can be summarized as illustrated in Fig. 8. For the design of practical superhydrophobic surfaces, a suggestion from this criterion is that a suitable pillar height, i.e., higher than the critical height but not too much higher, is necessary to guarantee such a transition and to prevent surface microtextures from breaking or damage (an excessively tall texture can be susceptible to breakage). Here it should be pointed that the significant role of critical pillar height is also indicated by other studies, e.g., the recent experimental observation by Fürstner et al. [18] and model studies by Carbone and Mangialardi [44].

3.2. The effects of pillar width and spacing (or solid fraction)

3.2.1. The effect of pillar width on FEB and FE

To investigate the role of pillar width, we fix all other parameters and only vary the pillar width (pillars have a square cross section). Fig. 9 illustrates the normalized FEBs for noncomposite

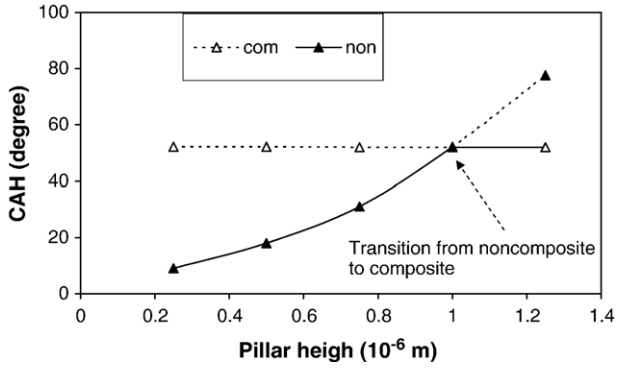

Fig. 8. Variations of CAH with respect to pillar height for a wetting system with $L=1\times10^{-2}$ m, $a=b=2$ μm; intrinsic CA, $\theta_Y=120°$. Solid lines represent plausible variations of CAH, whereas dashed lines represent CAH variations if wetting system with high FE values were permissible. *non* and *com* denote noncomposite and composite states, respectively. The lines are to guide the eyes [41].

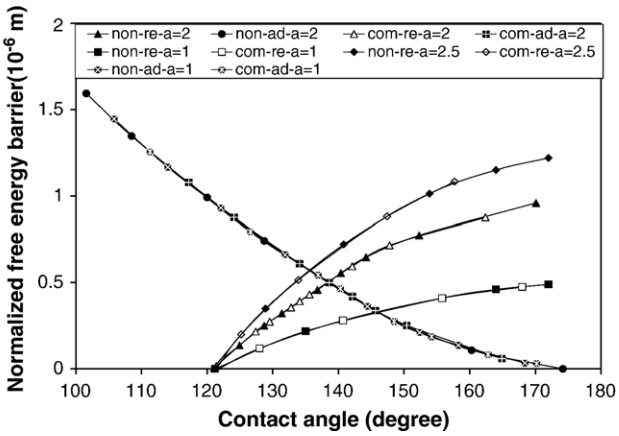

Fig. 9. Variations of normalized FEB with apparent CA for various pillar widths of the microtextured surfaces for noncomposite and composite wetting states; $L=1\times10^{-2}$ m, $h=1$ μm, $b=2$ μm; intrinsic CA, $\theta_Y=120°$; the unit for a is micrometers. *non* and *com* denote noncomposite and composite states; *re* and *ad* denote receding and advancing, respectively. The lines are to guide the eyes.

state with different pillar widths. One can see that receding FEB increases with increasing pillar width, whereas advancing FEB does not depend on pillar width. The intersection of receding and advancing FEB curves corresponds to the Wenzel's CAs. It is important to note that for the noncomposite system, all of the receding curves cross the x-axis at the CA of 120°. This implies that the receding CA for this system does not depend on pillar width. This happens because the vibrational energy is assumed as zero in the present study. However, if the vibrational energy is not zero, the receding CA depends strongly on pillar width (see below).

Fig. 9 also illustrate the FEBs of composite systems with different pillar widths. One can see that both the receding and advancing FEB curves of noncomposite and composite states with different pillar widths overlap. Calculations of FE for noncomposite and composite states confirm the same results, i.e., the FE curves of both noncomposite and composite states with different pillar widths overlap, as illustrated in Fig. 10.

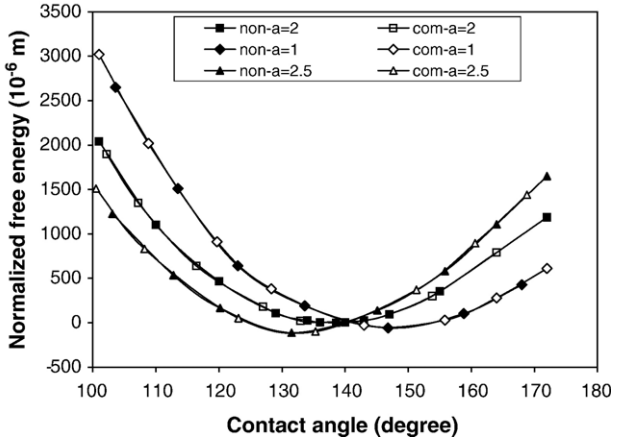

Fig. 10. Comparison of variations of normalized FE with apparent CA between noncomposite and composite wetting states with different pillar widths; the unit for a is micrometers; the other geometrical dimensions are: $L=1\times10^{-2}$ m, $h=1$, $b=2$ μm; intrinsic CA, $\theta_Y=120°$. *non* and *com* denote noncomposite and composite states, respectively. The lines are to guide the eyes.

This implies that for the transition between noncomposite and composite states in the current system the combination of pillar spacing and height (b=2 and h=1 μm) is more important than the change in pillar width (see Fig. 11). Furthermore, the same FE and FEB profiles for noncomposite and composite states means that the equilibrium CA for noncomposite and composite systems will be the same, i.e., Wenzel's CA is equal to Cassie's CA. Using Eqs. (17) and (18) as well as Wenzel's and Cassie's equations, it is confirmed that for the given system (b=2 and h=1 μm), Wenzel's CA is always equal to Cassie's CA no matter how pillar width changes.

3.2.2. The effect of solid fraction on FEB and FE

It should be pointed out that relative values rather than absolute values for surface texture geometry play a significant role in wetting behavior. As seen from Eqs. (17) and (18), pillar width affects not only solid fraction but also roughness, whereas pillar height only affects roughness. Thus, the effect of solid fraction cannot be explicitly demonstrated using absolute values of pillar width. To better understand the role of solid fraction (f), both pillar width and spacing are changed at the same time to obtain different f values in the following calculations. Note that the sum of pillar width (a) and spacing (b), is kept constant, and pillar height (h) is fixed to keep roughness constant.

Fig. 12 illustrates the FEBs for noncomposite systems with different f values of 0.375, 0.5 and 0.625. One can see that all the receding FEB curves cross at the CA of 120°; both the receding and advancing FEB curves shift upward with increasing f value (increasing pillar width or decreasing pillar spacing) when apparent CA is greater than 120°. One can also see that the intersecting points (i.e., equilibrium CAs) between the receding and advancing FEB curves have the same CA value, indicating independence of the equilibrium CA from solid fraction; this value exactly corresponds to the Wenzel's CA. This indicates that the texture geometry does not affect the equilibrium CA as long as the roughness value remains constant. It is also noted that the receding CAs do not depend on solid fraction, whereas the advancing CAs increase with increasing solid fraction. As a result, CAH also increases with increasing solid fraction. Here note that the above theoretical results are consistent with the latest experimental observations. For example, Callies et al. [17] investigated the effects of solid fraction on various CAs (receding, advancing, and equilibrium as well as CAH) for both noncomposite and composite states in detail. They showed that both the receding and the equilibrium CAs for noncomposite states remained almost unchanged with increasing solid fraction, whereas the advancing CA increased notably.

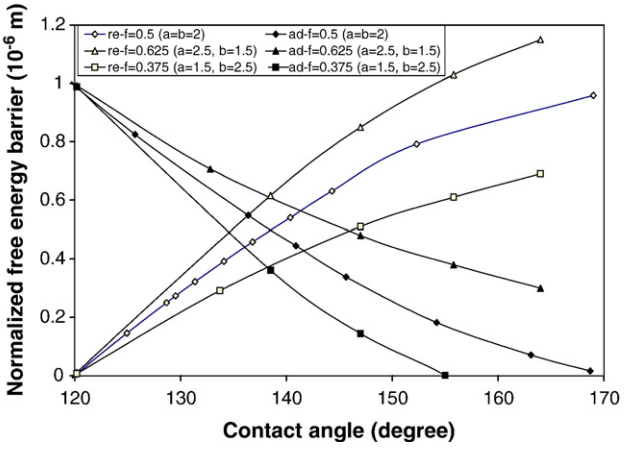

Fig. 12. Variations of normalized FEB with apparent CA for various pillar widths and spacing (solid fractions: f) for noncomposite states; $L=1\times10^{-2}$ m, h=1 μm; intrinsic CA, θ_Y=120°; the unit for a and b is micrometers; *re* and *ad* denote receding and advancing, respectively. The lines are to guide the eyes.

Fig. 13 illustrates the FEBs for a composite system with different solid fractions. One can see that the receding FEB increases with increasing solid fractions (indeed, the FEB curves for composite states are the same as those for noncomposite states). However, the advancing FEB decreases with increasing solid fractions and all the FEB curves cross the x-axis at about 173°. The equilibrium CA values, where each pair of FEB curves from receding and advancing intersect,

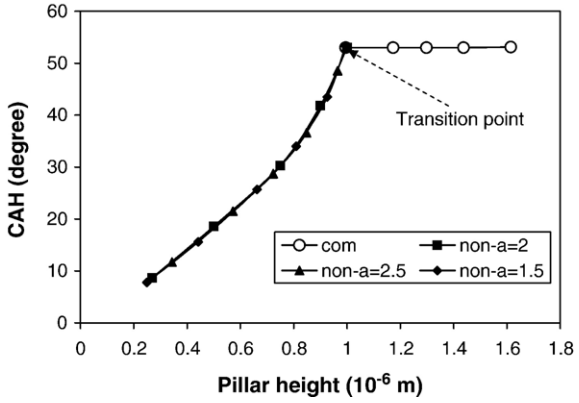

Fig. 11. Variation of CAH and transition from noncomposite (*non*) to composite (*com*) states with respect to pillar width ($L=1\times10^{-2}$ m, b=2 μm; intrinsic CA, θ_Y=120°); the unit for a is micrometers.

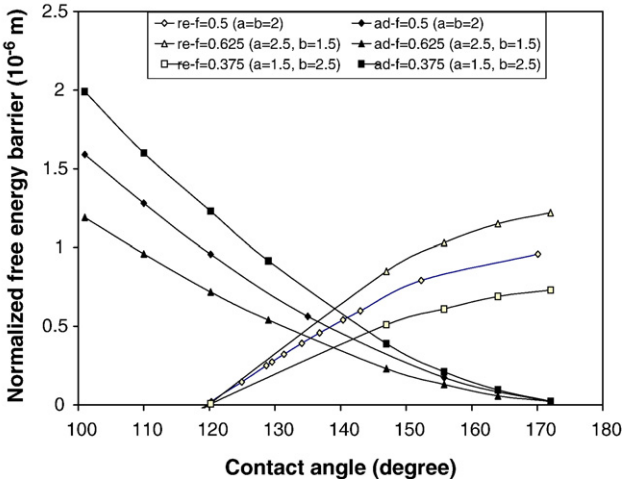

Fig. 13. Variations of normalized FEB with apparent CA for various pillar widths and spacing (solid fractions: f) for composite states; $L=1\times10^{-2}$ m, h=1 μm; intrinsic CA, θ_Y=120°; the unit for a and b is micrometers; *re* and *ad* denote receding and advancing, respectively. The lines are to guide the eyes.

decrease with increasing solid fractions. These CA values also exactly correspond to the Cassie's CAs. It is worth noting that for zero vibrational energy, neither of the receding and advancing CAs depends on solid fraction. Accordingly, CAH for composite states always remains unchanged for various solid fractions. Note here that in the experimental study of Callies et al. [17], for composite states, the advancing CA remained almost unchanged with increasing solid fraction, whereas the equilibrium CA decreased; this is also consistent with our above theoretical predictions. The decrease of receding CA for composite states are somewhat different from ours results. But by considering the effect of a small vibrational energy (see below) in our calculations, the receding CA will decrease, whereas the advancing CA will remain almost unchanged.

Fig. 14 illustrates the variations of FE with respect to CA for noncomposite and composite states with different solid fractions. One can see that all the FE curves for noncomposite states with different solid fractions overlap, i.e., the FE for noncomposite states does not depend on solid fraction, indicating an unchanged Wenzel's CA (the minimum FE locus). The FE curves for composite states can be higher or lower than those for noncomposite states, depending on the solid fraction; for different FE curves, locations of the minimum FE exactly correspond to the Cassie's CAs. It is noted that the FE increases with decreasing the solid fraction, indicating that a system with relatively thin pillars possesses higher FE and hence is not energetically preferable for composite states. This seems to be in disagreement with some recent understanding. For example, Patankar [7] theoretically demonstrated that to achieve superhydrophobicity, it is needed to make the ratio of pillar width to pillar height (a/h) very small, e.g., tall and slender pillars with appropriate spacing. However, our results show that a higher FE is observed for the lower solid fraction as a result of an increase in pillar spacing (note that r is kept constant). To understand this key point, it is necessary to focus on trough width, where the penetration of liquid occurs, rather than pillar height. If pillar height remains unchanged, the larger the trough

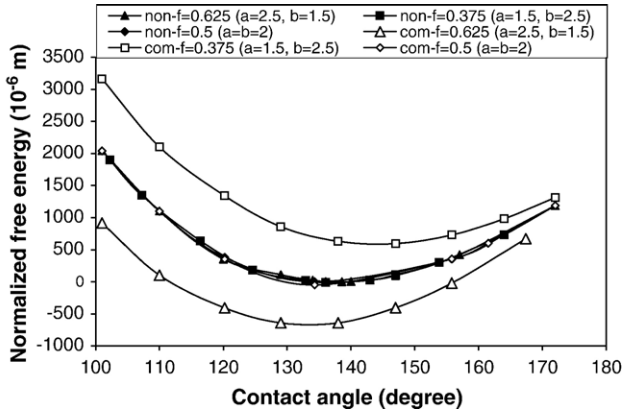

Fig. 14. Comparison of variations of normalized FE with apparent CA between noncomposite (*non*) and composite (*com*) wetting states with different pillar widths and spacing (solid fractions: f); the unit for a and b is micrometers; the other geometrical dimension are: $L=1\times10^{-2}$ m, $h=1$ μm; intrinsic CA, $\theta_Y=120°$. The lines are to guide the eyes.

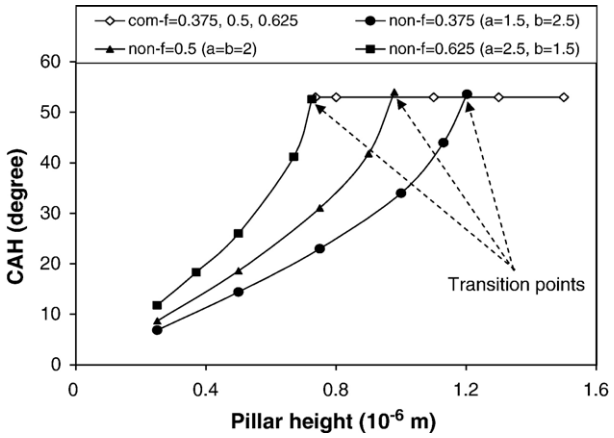

Fig. 15. Variation of CAH with respect to pillar widths and spacing (solid fractions) ($L=1\times10^{-2}$ m; intrinsic CA, $\theta_Y=120°$); the unit for a and b is micrometers. *non* and *com* denote noncomposite and composite states, respectively. The lines are to guide the eyes.

width (pillar spacing), the smaller the capillary force, and the easier the drop penetrates into troughs, i.e., increasing the trough width or decreasing the trough (pillar) height plays a similar role in determining composite (superhydrophobic) state. This simply indicates that composite state is mainly observed as a result of manipulating pillar spacing and not necessarily pillar dimension for the given geometry.

Fig. 15 illustrates the variations of CAH for noncomposite and composite states with different solid fractions. The CAH for composites states remains unchanged no matter how the geometrical parameters of the system change, whereas the CAH for noncomposite states increases sharply with respect to pillar height with small pillar spacing (or the large solid fraction).

3.2.3. The effect of pillar spacing and solid fraction on the wetting transition

Recalling the role of the pillar width in FE and FEB as well as CAH without changes in other geometrical parameters (see Figs. 9–11); we find that pillar width has no effect on the transition. The transition is only related to pillar height and spacing for a given texture. However, such independence of the transition from pillar width does not mean the independence of superhydrophobicity from pillar width. In fact, pillar width plays an important role in practical cases with non-zero vibrational energy. As shown in Figs. 13 and 14, small pillar width (thin pillars) can lead to a high equilibrium (stable) CA. Thus, when there is an external source of energy, i.e., a non-zero vibrational energy, superhydrophobic behavior (high stable CA and low CAH) for practical wetting systems can be easily realized (see below). Furthermore, we find that the transition depends strongly on pillar height relative to pillar spacing (i.e., h/b) rather than pillar width (i.e., h/a) as proposed by Patankar [7]. Since the FE curves of noncomposite and composites states for the system with $h=1$ and $b=2$ μm overlap, we can extend the previous critical pillar height to relative critical pillar height (h_c^r) and therefore propose a more general criterion

for the transition between noncomposite and composite wetting states as:

$$h/b \geq h_c^r \quad (24)$$

Examining the data in Fig. 16, it is found that the texture dimensions ($b=1.5$ μm, and $h=0.75$ μm) exactly meet the present criterion: $h_c^r=0.5$ for the system studied. In addition, the present criterion also indicates that solid fraction does not impact the transition as long as the relative pillar height remains unchanged.

Here it should be pointed out that regarding the criterion for the transition, i.e. Eq. (24), experimental investigators have found the critical role of small pillar spacing. For example, Fürstner et al. [18] and Nakae et al. [16] believed that narrow pitch (i.e., small spacing) or a roughness pitch smaller than a critical value can result in the transition, whereas Callies et al. [17] suggest that high densities (i.e., small spacing) cannot lead to the Wenzel state. These results support our suggestion that a criterion based on h/b rather than the h/a proposed in [7] is more appropriate for transition. Furthermore, it is revealed that for a roughness pitch less than a critical value, the CA increases with the pitch, whereas for a roughness pitch larger than the critical value, the (equilibrium) CA decreases with the pitch because the liquid can "touch" the bottom of the through [16]. Based on the present theoretical analysis, this is easily understood that the key role pillar spacing is playing in the transition when pillar height is kept constant. For a given pillar height, an adequately small spacing can result in a composite state; for the resultant composite state, the larger the spacing, the larger the CA, i.e. right after transition the conditions are such that the largest CA will be observed for the current surface texture design. In contrast, a large spacing can result in a noncomposite state; for the resultant noncomposite state, the larger the spacing, the smaller the CA. This indicates the consistency of our theoretical analysis with the above experimental observations. In addition, it is interesting to note that in Fürstner et al. experimental observation [18], they changed only one parameter (e.g., spacing) while keeping other two parameters (e.g., height and width) unchanged in order to understand the role of each geometrical parameter of a surface microtextured with spikes. They used sliding angles that with caution, this data may be interpreted in terms of CAH to allow us to make a comparison between their result and our theoretical predictions. They demonstrated that the sliding angle for noncomposite states with decreasing spacing (or increasing pillar width) increased except for certain values, whereas sliding angles for composite states remained almost unchanged. This indicates a basic agreement with the above theoretical results (Fig. 15).

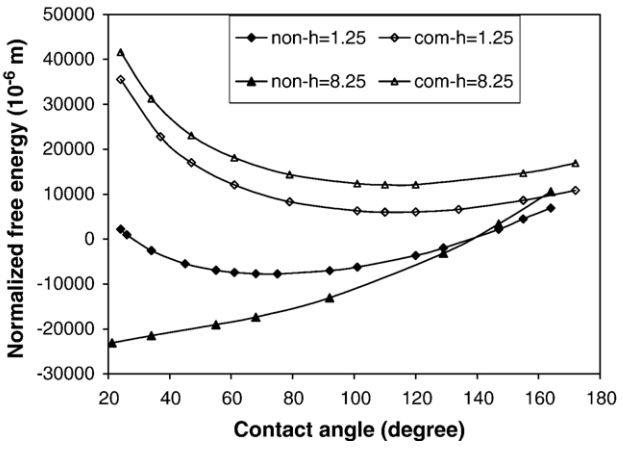

Fig. 16. Variations of normalized FE with apparent CA of noncomposite and composite wetting states with different pillar heights (h); $L=1\times10^{-2}$ m, $a=b=2$ μm; intrinsic CA, $\theta_Y=80°$; the unit for h is micrometers. *non* and *com* denote noncomposite and composite states, respectively. The lines are to guide the eyes.

Based on the discussion in this section, the present study gives a clear thermodynamic explanation on how thin and tall microtextures affect the superhydrophobic performance. This also indicates that a re-consideration of the previous suggestion for the transition, as demonstrated above, is required. Especially, the revised criterion is extremely important for the design of superhydrophobic surfaces. For example, regarding the practical concern of strength or durability of surface textures, a suggested strategy is to use small pillar spacing rather than small pillar width in order to gain composite (superhydrophobic) state.

3.3. The effect of intrinsic CA

3.3.1. The effect of intrinsic CA on FE

The discussions above were for application of hydrophobic materials (i.e., intrinsic CA larger than 90°). In this section, we focus on how some of the above findings may be very different should the intrinsic CA be smaller than 90° (note that the effect of intrinsic CA is based on a specific surface texture presented here).

Fig. 16 shows variations of normalized FE with respect to apparent CA for the system with an intrinsic CA of 80° with different pillar heights ($a=b=2$ μm). One can see that compared with the system with an intrinsic CA larger than 90° (Fig. 6), the FE of composite states for the present system is always higher than that of noncomposite states for any pillar height. This means that noncomposite states for this system are more stable than composite states, especially when the apparent CA is low and the pillar height is large. Moreover, when pillar height is small (e.g., $h=1.25$ μm), the calculated equilibrium CA (with lowest FE), θ_e, of noncomposite state exactly corresponds to that predicted by Wenzel's equation, which is smaller than the intrinsic CA and decreases with an increase in pillar height. However, when pillar height is large enough (e.g., $h=8.25$ μm), there is no minimum FE for a noncomposite state, which means sufficiently high pillar height can lead to the surface wicking (as discussed in detail in the J–D model [28]). The θ_e of composite state also exactly corresponds to the predicted value by Cassie's equation, which is larger than the intrinsic CA and does not depends on pillar height. For an intrinsic CA smaller than 90° (e.g., 30° or 60°), the same trend of FE variations with respect to CA is found.

Fig. 17 shows variations of normalized FE with respect to apparent CA for a system for the specific case of an intrinsic CA of 90° for different pillar heights. One can see that FE curves of

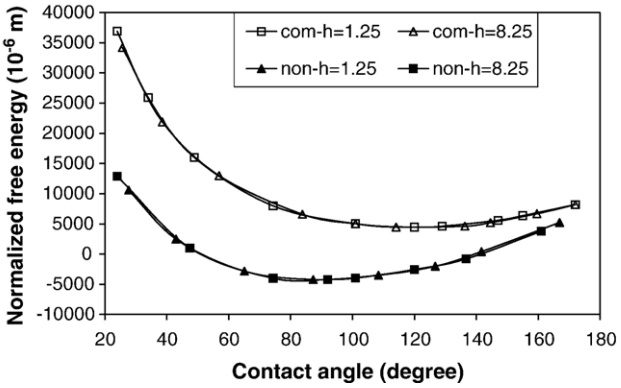

Fig. 17. Variations of normalized FE with apparent CA of noncomposite (*non*) and composite (*com*) wetting states with different pillar heights (h); $L=1\times10^{-2}$ m, $a=b=2$ μm; intrinsic CA, $\theta_Y=90°$; the unit for h is micrometers. The lines are to guide the eyes.

both noncomposite and composite states overlap. This implies that for this special intrinsic CA, FE variations do not depend on pillar height, i.e. the FE of a composite and a noncomposite system will be equal and these two states can coexist (also see below). From Fig. 18 one can see that the FE curve for CA of 90° is the limiting case between that of composite and noncomposite states i.e., when either of these states would be energetically favorable. Since the two FE curves of both noncomposite and composite states for the intrinsic CA of 90° are the closest, from a thermodynamic point of view, such system can exhibit the largest possibility for the transition from noncomposite to composite states or vice versa. Compared with intrinsic CA, pillar height can have an opposite effect on the FE for the system with an intrinsic CA smaller than 90°, i.e., FE of noncomposite states dramatically decreases with pillar height, whereas FE of composite states dramatically rises with pillar height. It is also noted that FE curves of noncomposite states are farther spaced than those for composite states, especially for the systems with a small intrinsic CA and a large pillar height. This implies that the FE of noncomposite states is more sensitive to intrinsic CA and pillar height than that of composite states. Therefore, once composite state is achieved (mainly seen in superhydrophobic surfaces) there is no need to have excessively tall pillars that would compromise the mechanical durability of the surface texture.

3.3.2. The effect of intrinsic CA on FEB

Fig. 19 compares the effect of different intrinsic CAs (80°, 90°, and 110°) on normalized FEB. For the system with an intrinsic CA smaller than 90°, advancing FEB or CA remains unchanged with respect to the pillar height; it should be noted that in the previous section it is shown that for the system with an intrinsic CA larger than 90°, receding FEB or CA remains unchanged. Furthermore, the CA at the intersection of the two curves corresponds to Wenzel's CA, which is smaller than the intrinsic CA (e.g. in Fig. 19, the advancing and receding FEB curves intersect at an apparent CA value less than $\theta_Y=80°$). For systems with θ_Y less than 90°, the negative FEB values represent a "barrier" for moving from one metastable local to the next, whereas for systems with θ_Y larger than 90° the positive values represent a "barrier". This stems from our sign convention in our calculations (note that if θ_Y is less than 90° a positive value of FEB means no "barrier", whereas for cases with θ_Y larger than 90° a negative value of FEB means no "barrier" to movement of contact line).

For the system with an intrinsic CA of 90°, Wenzel's CA is also 90°. It is interesting to note that the two curves also

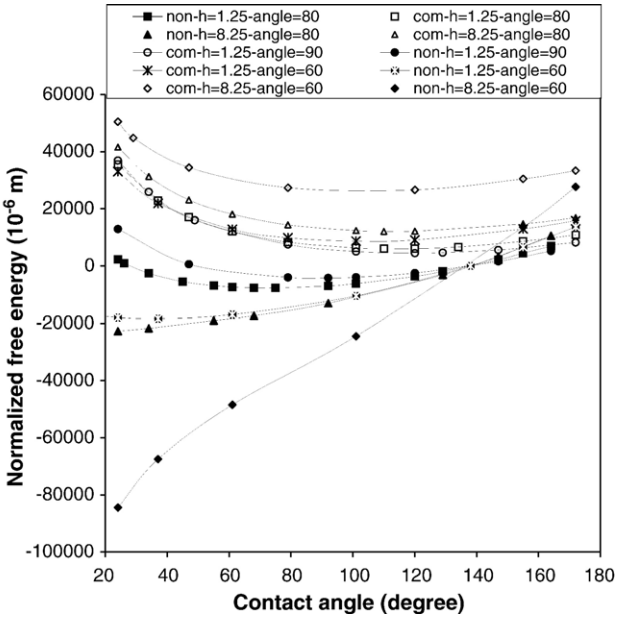

Fig. 18. Comparison of variations of normalized FE with apparent CA for systems with various intrinsic CAs and pillar heights (h); $L=1\times10^{-2}$ m, $a=b=2$ μm; the unit for h is micrometers. *non* and *com* denote noncomposite and composite states, respectively. The lines are to guide the eyes.

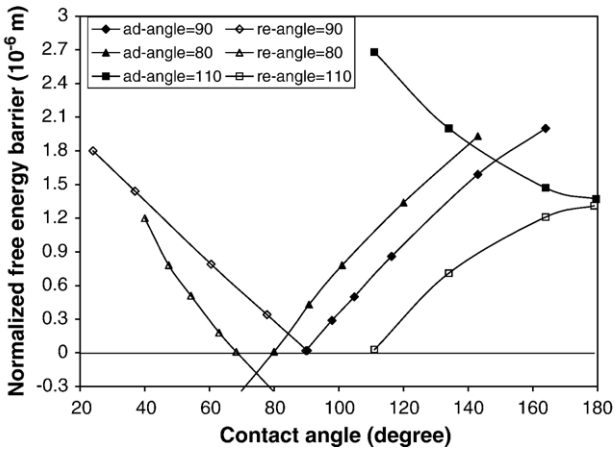

Fig. 19. Variations of normalized FEB with apparent CA for noncomposite wetting systems with intrinsic CAs, $\theta_Y=110°$,$\theta_Y=90°$, and $\theta_Y=80°$; $L=1\times10^{-2}$ m, $h=1$, $a=b=2$ μm; *re* and *ad* denote receding and advancing, respectively. Note that for systems with θ_Y less than 90°, the negative FEB values represent a "barrier" for moving from one metastable local to the next, whereas for systems with θ_Y larger than 90° the positive values represent a "barrier" (note that if θ_Y is less than 90° a positive value of FEB means no "barrier", whereas for cases with θ_Y larger than 90° a negative value of FEB means no "barrier" to movement of contact line); this stems from our sign convention in our calculations. The lines are to guide the eyes.

intersect at apparent CA of 90° where both advancing and receding FEBs are zero. This means that CAH for this system is zero. In addition, for the system with an intrinsic CA larger than 90° (e.g., 110°), when pillar height exceeds a certain value, for example, $h=4$ μm advancing and receding curves do not intersect any longer; advancing curve does not intersect at zero FEB either. In terms of the Wenzel's equation, this means that roughness factor is so high that $\cos\theta_w>1$. In this case, the advancing CA for the system could be assumed as 180°, and receding CA can be found by intersection of receding FEB curve with the x-axis.

3.3.3. The effect of intrinsic CA on CAH and wetting transition

Fig. 20 shows variations of CAH for various noncomposite and composite systems with intrinsic CA and pillar height. Intrinsic CA is an important factor in determining the magnitude of the CAH. For composite states (i.e., horizontal lines in Fig. 20) CAH decreases with the increase in intrinsic CA. CAH for such systems is insensitive to the surface texture geometry, e.g. pillar height as shown in Fig. 20. Comparatively, variations of CAH with intrinsic CA for noncomposite systems are complex. This complexity partly arises from the fact that CAH is not constant for noncomposite systems as it is for composite systems; and it depends on pillar height or generally surface texture geometry. The curves can be divided into two categories: one for intrinsic CA larger than 90°; another for intrinsic CA smaller than 90°. For noncomposite systems with the intrinsic CA larger than 90°, the larger the intrinsic CA, the faster the CAH increases due to an increase in pillar height. However, when the intrinsic CA is smaller than 90°, e.g., 80°, CAH increases slowly with an increase in the pillar height. Therefore, if there is a transition from noncomposite to composite state, the CAH would be smaller for cases were intrinsic CA is larger than 90° compared to the case where intrinsic CA is smaller than 90° (compare the curves for CA of 80° and 120° in Fig. 20). It should however be noted that for cases where intrinsic CA is less than 90° since the FE of composite system is higher than that of noncomposite states (see Fig. 18), the noncomposite state is preferable and there is no transition possible for the microtexture geometry defined.

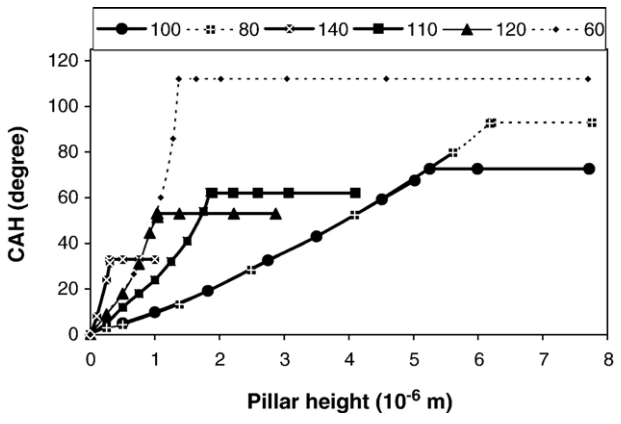

Fig. 20. Thermodynamically plausible variations of CAH versus the pillar height for systems with various intrinsic CAs; $a=b=2$ μm.

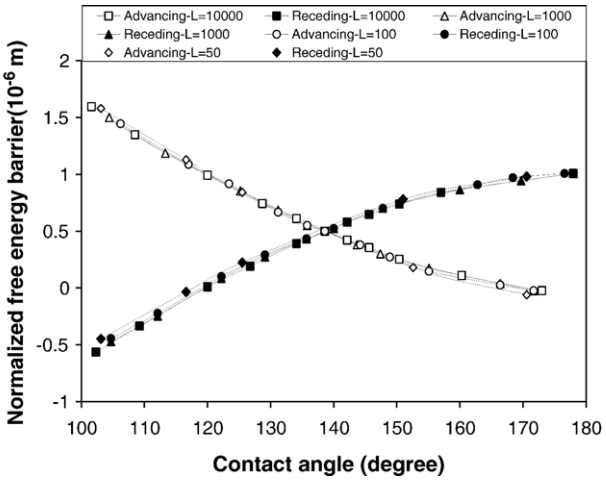

Fig. 21. Variations of normalized FEB with apparent CA for various drop sizes (L) in noncomposite wetting systems; $h=1$, $a=b=2$ μ m; intrinsic CA, $\theta_Y=120°$; the unit for L is micrometers. The lines are to guide the eyes.

Based on the above discussion, practically plausible variations of CAH versus pillar height of various systems with various intrinsic CAs can be represented by the solid curves in Fig. 20, whereas the dashed curves may be impossible.

The above results indicate that intrinsic CA also affects the possibility of the transition between noncomposite and composite states. There is some experimental data that suggests, to the contrary of our findings, that composite state is plausible for a system with an intrinsic CA smaller than 90° [45,46]. In these studies, hydrophilic surfaces (intrinsic CA of 70° [45] or 77° [46]) were employed, but a transition from noncomposite to composite states was shown as the depth of surface topography pores (a similar parameter to the pillar height in the present work) was very large or reached a critical value. This, however, maybe explained by consideration of line energy that is not included in the current study [42].

3.4. The effect of drop size

Fig. 21 illustrates variations of normalized FEB with apparent CA for various drop sizes (L) for a noncomposite system ($a=b=2$, $h=1$ μm, $\theta_Y=120°$). One can see that all the FEB curves overlap, if L is larger than 50 μm, indicating independence of CA variation for large drops (compare to size of surface features). For the texture design here, similar trend can be found for a composite state. However, when L is close to pillar size, the drop size does affect the FEB. Fig. 22 shows variations of advancing and receding CAs with respect to drop size for the noncomposite system. One can see that both receding and advancing CAs remain unchanged when drop size is about two orders of magnitude larger than pillar size; both receding and advancing CAs change when drop size approaches pillar size; the decreases in receding and advancing CAs are about 6° and 11°, respectively. To completely understand the effect of drop size, calculations were done for other wetting systems. For the noncomposite system with various pillar heights or intrinsic CAs, a similar trend for the dependence of CAs on drop size was found. The above results indicate that

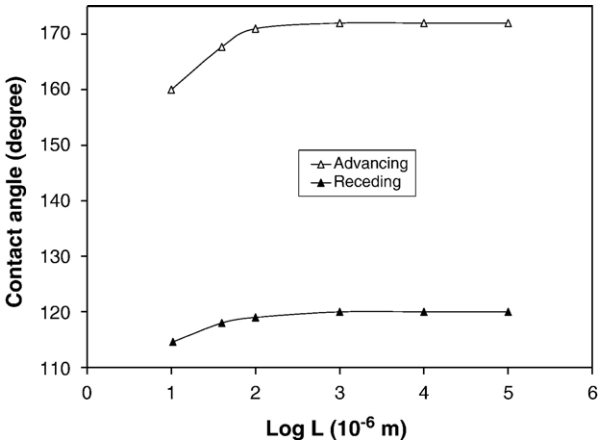

Fig. 22. Variations of advancing and receding CAs with respect to drop size (L) for the microstructure surfaces in noncomposite wetting systems; h=1, a=b=2 μm; intrinsic CA, θ_Y=120°. The lines are to guide the eyes.

superhydrophobic behavior can be affected for small drops that are comparable in size with surface microtextures. This is particularly important for micro/nano-scale drops in microfluidic devices.

3.5. Vibrational energy effect

The above calculations and discussions are based on the assumption that in an ideal case, the vibrational energy is equal to zero. However, the vibrational energy as defined earlier (and according to the J–D model [28]) may not necessarily be zero. This is also shown experimentally, e.g. [34]. Regardless of the physical nature of the vibrational energy, in the present study it is important to investigate how the vibrational energy affects receding and advancing CAs as well as CAH. As illustrated in Fig. 5, plausible vibrational energy for the given system may vary from 0 (ideal case) to 0.36 μm (the corresponding value at intersecting point of advancing and receding FEB curves, i.e., equilibrium locus); note that for consistency, vibrational energy is also normalized, and its unit is also meter. Thus, CAH varies from a maximum (31°) to a minimum (0°). Fig. 23 illustrates

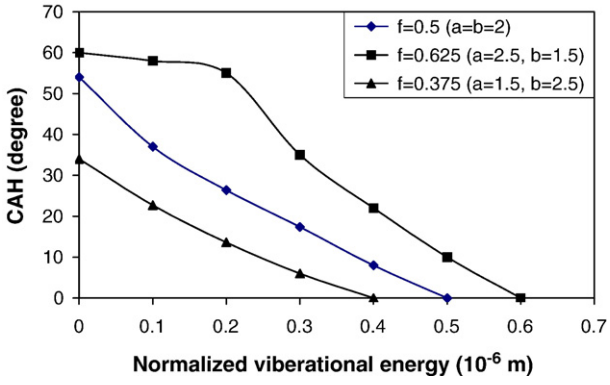

Fig. 23. Variations of CAH for noncomposite states with respect to the normalized vibrational energy; the unit for a and b is micrometers. Intrinsic CA, θ_Y=120°; f is solid fraction. The lines are to guide the eyes.

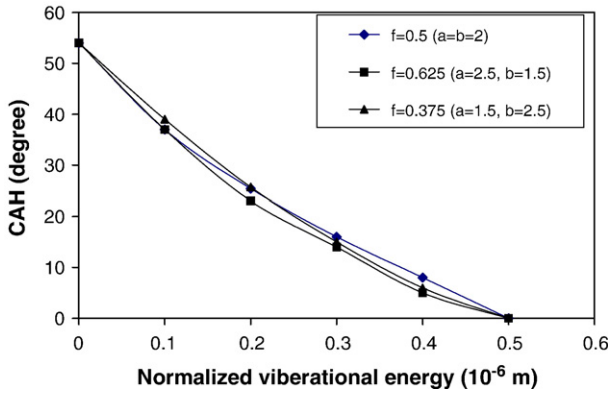

Fig. 24. Variations of CAH for composite states with respect to the normalized vibrational energy; the unit for a and b is micrometers. Intrinsic CA, θ_Y=120°; f is the solid fraction. The lines are to guide the eyes.

variations of CAH for noncomposite states with various vibrational energy levels for a system with θ_Y>90°. One can see that in general, CAH decreases with increasing vibrational energy. In general terms, this is consistent with the experimental results in [34] and [36] for heterogeneous and/or rough surfaces. One can also see that for a given vibrational energy level, CAH increases with an increase in solid fraction (f); note that the roughness ratio remains unchanged in the present case. However, in a composite state, surface exhibits a somewhat different trend for CAH, as illustrated in Fig. 24. One can see that CAH decreases with increasing vibrational energy but hardly depends on the solid fraction.

In case of the change in surface chemistry (intrinsic CA), the effect of the vibrational energy on CAH remains the same, i.e. with increased vibrational energy, the CAH will decrease and eventually reach zero (see Fig. 25). It should be noted that in Fig. 25, the absolute value of FEB is plotted, since a negative value of FEB indicates a "barrier" for systems with θ_Y less than 90 in contrast to cases with θ_Y larger than 90 that a positive value of FEB represents a "barrier" (this is due to the sign convention used in our calculations).

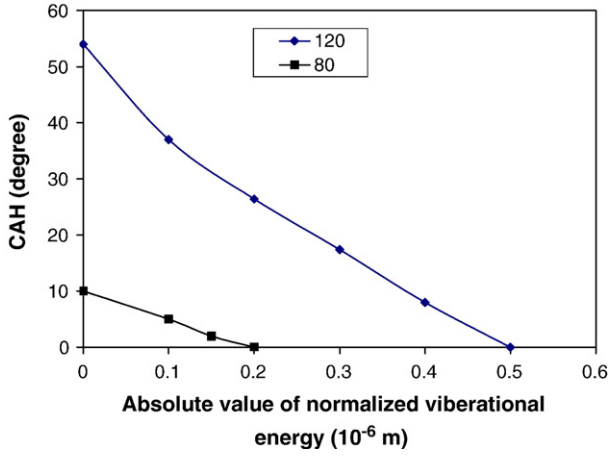

Fig. 25. Variations of CAH of noncomposite states for different intrinsic CAs with respect to the absolute value of the normalized vibrational energy (see Section 3.5).

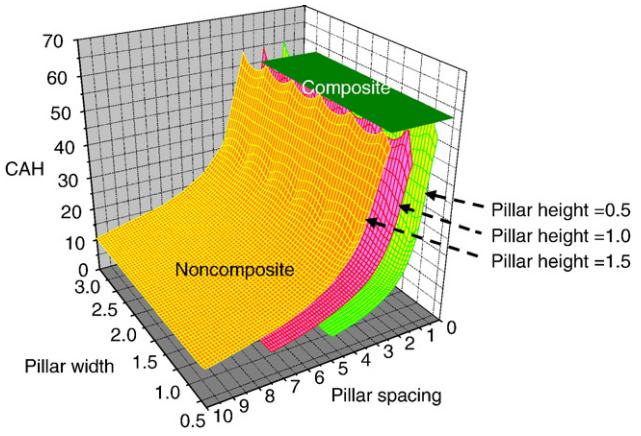

Fig. 26. CAH as a function of pillar width, height, and spacing for a system with an intrinsic CA of 120°.

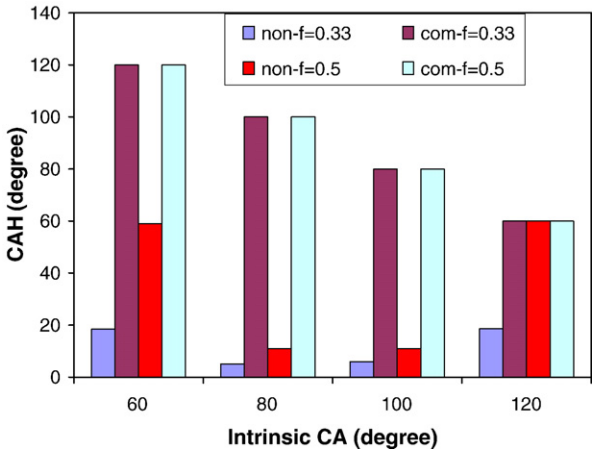

Fig. 28. Comparison of CAH as a function of solid fraction (f) for various intrinsic CAs; *non* and *com* denote noncomposite and composite states, respectively.

From the above results, it becomes clear that the effect of vibrational energy on the superhydrophobic behavior can depend on both the surface texture dimension and chemistry. However, to fully understand the physical nature of above findings, experimental studies similar to ones in [34–36] are needed, but specific for textured surfaces (i.e. fabricating various model textured surfaces and subjecting them to mechanical vibrations to verify the relations between surface texture geometry and CAH as predicted here).

3.6. Concurrent effect of various parameters

The basic approach employed in the present study was to investigate one at a time the primary parameters in determining superhydrophobic behavior. As a summary, here we discuss the concurrent effect of various parameters on CAH to gain a comprehensive understanding, with an emphasis on the surface geometry. Fig. 26 illustrates variations in CAH for a system with an intrinsic CA of 120°. As shown, for the noncomposite state, pillar width and spacing hardly affect CAH when pillar height is low, but as pillar height increases, its role becomes prominent. As a result, the larger the pillar height, a larger pillar spacing is needed for the transition from a noncomposite to a composite state. However, for an intrinsic CA of 60°, there is no such transition no matter how pillar width and spacing is changed, as shown in Fig. 27. This further stresses the crucial role of intrinsic CA in determining the transition, as demonstrated in the above calculations based on a constant summation for pillar width and spacing (i.e. $a+b=$const.). To further demonstrate the effects of solid fraction and roughness, Figs. 28 and 29 illustrate a comparison of CAH for various intrinsic CAs. One can see that the CAH for composite states is higher than that for noncomposite states until the intrinsic CA reaches 120° no matter how solid fraction or roughness ratio is changed. This implies that for the presented surface microtexture, composite or superhydrophobic states are almost unstable or energetically unfavorable since the intrinsic CAs of materials is always smaller than 120°. Thus, the present study emphasizes an important conclusion that in most cases, the transition from a noncomposite to composite state is usually difficult unless intrinsic CA is large enough. To demonstrate the concurrent

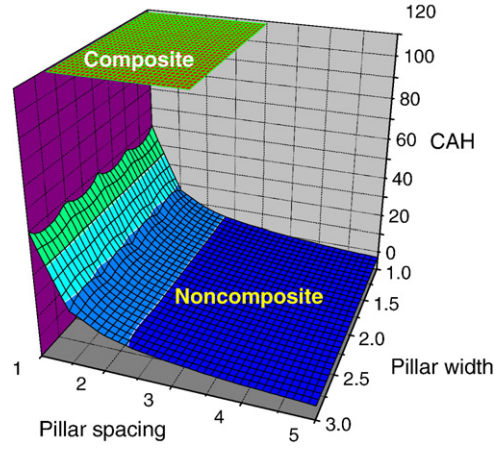

Fig. 27. The transition in CAH as a function of pillar width and spacing for a system with an intrinsic CA of 60°and pillar height of 1 μm.

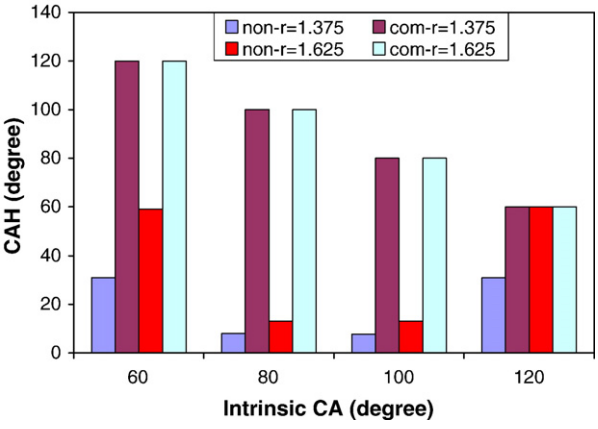

Fig. 29. Comparison of CAH as a function of roughness ratio (r) for various intrinsic CAs; *non* and *com* denote noncomposite and composite states, respectively.

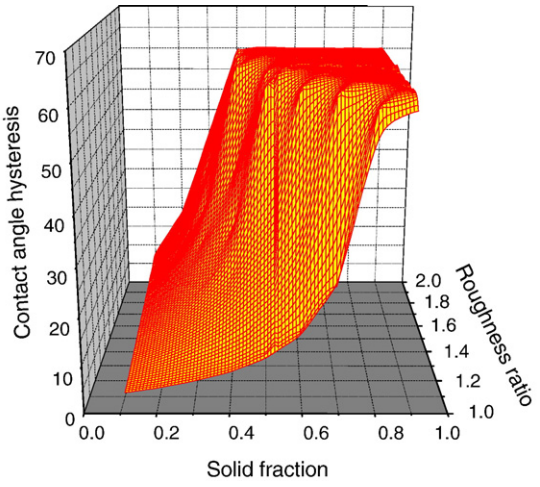

Fig. 30. The transition in CAH as a function of solid fraction and roughness ratio between noncomposite and composite states. The intrinsic contact angle is 120°.

effects of all the geometrical parameters on transition between noncomposite and composite states, a plot of CAH as a function of solid fraction and roughness ratio can be examined (Fig. 30).

3.7. The basic guidelines for design of superhydrophobic surfaces

The present study reveals that even if a wetting system with zero-vibrational energy is in composite state, receding and advancing CAs do not depend on surface texture dimension. As a result, the CAH for this system cannot be lowered by changing surface texture dimension alone. However, receding and advancing CAs as well as CAH may change dramatically with the vibrational energy. Thus, based on the consideration of the vibrational energy we propose that for a practical superhydrophobic surface it is necessary to achieve a large equilibrium CA (instead of advancing or maximum CA) and small CAH, so that drop adhesion can be minimized for self-cleaning or water-repellent properties. Another key point is that even for a composite state, the minimum CAH for the system studied is about 60°due to practical available maximum intrinsic CA of 120°. However, CAH of 60° is a theoretical upper bound for the studied texture and may be minimized even to reach zero by imposing suitable vibrational energy. This also indicates the uncertainty of superhydrophobicity because of its dependence on external sources. Such uncertainty can, however, be exploited to have surfaces with tunable wettability.

The general principles for the design of superhydrophobic surfaces based on the present study are as follows:

(1) To meet the proposed geometrical criterion, adequately large roughness (high pillars), if trough geometry (i.e., pillar spacing and height) remains unchanged, is needed to reach a composite state. Large intrinsic CA is needed to guarantee a stable composite state.
(2) Small solid fraction (thin pillars) is needed to achieve a large equilibrium CA.
(3) Large intrinsic CA is needed to minimize CAH.
(4) Small pillar spacing is needed for composite states, whereas large pillar spacing is needed for large stable CA; to achieve large CA and small CAH simultaneously, a compromise between pillar spacing and other geometrical parameters such as pillar height and width spacing is therefore necessary.
(5) Compromise in designing for surface texture and chemistry may be needed to meet other demands of surface properties such as mechanical durability and/or optical transparency. For example, thin pillars are always beneficial to superhydrophobicity, in particular to large stable CA. However, if one is concerned with the strength of microtextures, using a large trough width, instead of extremely small pillar width is a better choice; dual scale texture can be helpful to meet some of the competing requirements.

Acknowledgements

The financial assistance of Natural Science and Engendering Research Council of Canada, Alberta Science and Research Authority, Canada Research Chair Program, and Petro-Canada Young Innovator Award are acknowledged.

References

[1] Barthlott W, Neinhuis C. Planta 1997;202:1.
[2] Neinhuis C, Barthlott W. Ann Bot 1997;79:667.
[3] Tavana H, Amirfazli A, Neumann AW. Langmuir 2006;22:5556.
[4] Öner D, McCarthy TJ. Langmuir 2000;16:7777.
[5] Bico J, Marzolin C, Quéré D. Europhys Lett 1999;47:220.
[6] Bico J, Tordeux C, Quéré D. Europhys Lett 2001;55:214.
[7] Patankar N. Langmuir 2003;19:1249.
[8] He B, Patankar N, Lee J. Langmuir 2003;19:4999.
[9] Miwa M, Nacajima A, Fujishima A, Hashimoto K, Watanabe T. Langmuir 2000;16:5754.
[10] Lee J, He B, Patankar NA. J Micromechanics Microengineering 2005;15:591.
[11] Wu X, Zheng L, Wu D. Langmuir 2005;21:2665.
[12] Lin F, Li S, Li Y, Li L. Adv Mater 2002;14:1857.
[13] Della Volpe C, Siboni S, Morra M. Langmuir 2002;18:1441.
[14] Nacajima A, Hashimoto K, Watanabe T. Monhefte Chem 2001;132:31.
[15] Yoshimitsu Z, Nakajima A, Watanabe T, Hashimoto K. Langmuir 2002;18:5818.
[16] Nakae H, Yoshida M, Yokota M. J Mater Sci 2005;40:2287.
[17] Callies M, Chen Y, Marty F, Pépin A, Quéré D. Microelectron Eng 2005;78–79:100.
[18] Fürstner R, Barthlott W, Neinhuis C, Walzel P. Langmuir 2005;21:956.
[19] Berim GO, Ruckenstein E. Langmuir 2005;21:7743.
[20] Chen Y, He B, Lee J, Patankar NA. J Colloid Interface Sci 2005;281:458.
[21] Wenzel RN. In Eng Chem 1936;28:988.
[22] Cassie ABD, Baxter S. Trans Faraday Soc 1944;40:546.
[23] Onda T, Shibuichi N, Satoh N, Tsuji K. Langmuir 1996;12:2125.
[24] Extrand CW. Langmuir 2002;18:7991.
[25] Extrand CW. Langmuir 2004;20:5013.
[26] Marmur A. Langmuir 2004;20:3517.
[27] Roura P, Fort J. Langmuir 2002;18:566.
[28] Johnson Jr RE, Dettre RH. Adv Chem Ser 1964;43:112.
[29] Lafuma A, Quéré D. Nat Mater 2003;2:457.
[30] Amirfazli A, Hanig S, Muller A, Neumann AW. Langmuir 2000;16:2024.
[31] Gaydos J, Neumann AW. J Colloid Interface Sci 1987;120:76.
[32] Li D, Neumann AW. Colloids Surf 1990;43:195.
[33] Marmur A. J Colloid Interface Sci 1994;168:40.

[34] Decker EL, Garoff S. Langmuir 1996;12:2100.
[35] Meiron TS, Marmur A, Saguy IS. J Colloid Interface Sci 2004;274:637.
[36] Della Volpe C, Maniglio D, Morra M, Siboni S. Colloids Surf A Physicochem Eng Asp 2002;206:47.
[37] Noblin X, Buguin A, Brochard-Wyart F. Eur Phys J E 2004;14:395–404.
[38] Russell TP. Science 2002;297:964.
[39] Feng X, Feng L, Jin M, Zhai J, Jiang L, Zhu D. J Am Chem Soc 2004;126: 62.
[40] Della Volpe C, Siboni S. J Colloid Interface Sci 1997;195:121.
[41] Li W, Amirfazli A. J Colloid Interface Sci 2005;292:195.
[42] Amirfazli A, Neumann AW. Adv Colloid Interface Sci 2004;110:121.
[43] Lou KKS, Bico J, Teo KBK. Nano Lett 2003;3:1701.
[44] Carbone G, Mangialardi L. Eur Phys J E 2005;16:67.
[45] Abdelsalam ME, Bartlett PN, Kelf T, Baumberg J. Langmuir 2005;21: 1753.
[46] Martires E, Seunarire K, Morgan H, Gadegaard N, Wilkirson CDW. Langmuir 2006;22:11230.